Computational and Structural Biotechnology Journal 27 (2025) 369–382

Contents lists available at ScienceDirect

Computational and Structural Biotechnology Journal

journal homepage: www.elsevier.com/locate/csbj

Research article

Plasticity of BioPhi-driven humanness optimization in ScFv-CD99 binding affinity validated through AlphaFold, HADDOCK, and MD simulations

Kanokporn Sornsuwan [a,b], Thanathat Pamonsupornwichit [b], On-anong Juntit [a,b], Weeraya Thongkum [a,b,c], Nuchjira Takheaw [d,e], Kanchanok Kodchakorn [a,f,*], Chatchai Tayapiwatana [b,e,**]

[a] Office of Research Administration, Chiang Mai University, Chiang Mai 50200, Thailand
[b] Center of Biomolecular Therapy and Diagnostic, Faculty of Associated Medical Sciences, Chiang Mai University, Chiang Mai 50200, Thailand
[c] Center of Innovative Immunodiagnostic Development, Department of Medical Technology, Faculty of Associated Medical Sciences, Chiang Mai University, Chiang Mai 50200, Thailand
[d] Biomedical Technology Research Center, National Center for Genetic Engineering and Biotechnology, National Science and Technology Development Agency at the Faculty of Associated Medical Sciences, Chiang Mai University, Chiang Mai 50200, Thailand
[e] Division of Clinical Immunology, Department of Medical Technology, Faculty of Associated Medical Sciences, Chiang Mai University, Chiang Mai 50200, Thailand
[f] Department of Chemistry, Faculty of Science, Chiang Mai University, Chiang Mai 50200, Thailand

ARTICLE INFO

Keywords:
BioPhi
Humanized ScFv
Binding affinity
AlphaFold
HADDOCK
MD simulations

ABSTRACT

BioPhi-guided humanization was utilized to enhance the humanness of a humanized single-chain variable fragment targeting CD99, leading to the development of two variants: HuScFvMT99/3^{BP} and HuScFvMT99/3^{HY}. The HuScFvMT99/3^{BP} variant incorporated framework region modifications, leading to modest improvements in humanness, particularly in the VH domain, although the VL domain remained suboptimal. To address this limitation, HuScFvMT99/3^{HY} was designed by combining the VL domain of wild-type with the VH domain of HuScFvMT99/3^{BP}. Molecular dynamics simulations employing AlphaFold2, AlphaFold3, and HADDOCK were performed to evaluate the HuScFv-CD99 peptide complexes. AF2-based simulations demonstrated enhanced binding free energy ($\Delta G_{binding}$) for both variants compared to HuScFvMT99/3^{WT}. However, $\Delta G_{binding}$ values obtained from AF3 and HD simulations were inconsistent, with HuScFvMT99/3^{BP} exhibiting the weakest binding affinity. While $\Delta G_{binding}$ patterns derived from AlphaFold3 and HADDOCK simulations aligned, amino acid decomposition analysis revealed variations in the interaction coordinates of the predicted complexes. Root-mean-square deviation analysis indicated improved structural stability for HuScFvMT99/3^{BP} (0.975 Å) and HuScFvMT99/3^{HY} (1.075 Å) relative to HuScFvMT99/3^{WT} (1.225 Å). Biolayer interferometry further confirmed that HuScFvMT99/3^{WT} exhibited the highest binding affinity ($K_D = 1.35 \times 10^{-7}$ M) compared to HuScFvMT99/3^{BP} ($K_D = 2.64 \times 10^{-7}$ M) and HuScFvMT99/3^{HY} ($K_D = 3.95 \times 10^{-7}$ M). Supporting evidence was provided by ELISA and flow cytometry experiments. PITHA analysis revealed a high immunogenicity risk for all variants, despite HuScFvMT99/3^{HY} displaying improved humanness, a larger complementarity-determining region (CDR) cavity, and a more hydrophobic CDR-H3 loop. These findings highlight the delicate balance between enhancing humanness and preserving the structural and functional integrity critical for therapeutic antibody development.

1. Introduction

Therapeutic antibodies have shown remarkable efficacy in treating cancers, autoimmune disorders, and infectious diseases by specifically targeting disease-associated antigens. [1–3] However, immunogenicity remains a significant challenge, as the patient's immune system may identify the antibody as foreign, thereby diminishing its therapeutic efficacy and potentially triggering adverse immune reactions. [4]

* Corresponding author at: Office of Research Administration, Chiang Mai University, Chiang Mai 50200, Thailand.
** Corresponding author at: Center of Biomolecular Therapy and Diagnostic, Faculty of Associated Medical Sciences, Chiang Mai University, Chiang Mai 50200, Thailand.
E-mail addresses: kanokporn.sornsuwan@cmu.ac.th (K. Sornsuwan), thanathat.pamon@cmu.ac.th (T. Pamonsupornwichit), Onanong.j@cmu.ac.th (O.-a. Juntit), weeraya.t@cmu.ac.th (W. Thongkum), nuchjira.t@cmu.ac.th (N. Takheaw), kanchanok.k@cmu.ac.th (K. Kodchakorn), chatchai.t@cmu.ac.th (C. Tayapiwatana).

https://doi.org/10.1016/j.csbj.2025.01.001
Received 26 November 2024; Received in revised form 2 January 2025; Accepted 4 January 2025
Available online 7 January 2025

Humanized antibodies are engineered to reduce immune responses by transferring complementarity-determining regions (CDRs) from non-human antibodies, typically mouse-derived, onto human antibody framework regions (FRs). [5] This approach retains the antigen-binding specificity of the non-human antibody while reducing its immunogenic potential. In cancer therapy, Trastuzumab, a humanized monoclonal antibody against human epidermal growth factor receptor 2 (HER2) has revolutionized the treatment of HER2-positive breast cancer, leading to tumor growth inhibition and improved patient outcomes. [6] Similarly, in autoimmune diseases, humanized antibodies like Tocilizumab inhibit the IL-6 receptor, relieving the symptoms of rheumatoid arthritis. [7] Despite their versatility and effectiveness, the human anti-human antibody (HAHA) induction by humanized antibody was observed in clinical trials, revealing further optimization for therapeutic humanized antibodies. [8,9]

Antibody humanization tools are indispensable for the development of humanized antibodies, as they ensure the retention of high specificity and affinity for target antigens while improving biocompatibility. [10, 11] The T20 score assesses the "humanness" of antibodies by calculating the percentage identity of the top 20 matching sequences within a human variable region sequence database. [12] However, this method is limited by its lack of data granularity and reliance on a small reference sequence set, which may restrict the diversity of the designed therapeutic antibody. Hu-mAb utilizes a random forest (RF) classifier trained on the Observed Antibody Space (OAS) database to differentiate between human and non-human sequences. [13] Since the OAS database primarily contains mouse and human origin sequences, this model performs poorly in classifying sequences from origins that it has not been trained. Recently, BioPhi, an open-source antibody design platform, has emerged as a robust solution for advancing the humanization and design of therapeutic antibodies. [14] This software features automated humanization methods, Sapiens, which utilizes deep learning on natural antibody repertoires for humanization, and Observed Antibody Space identity search (OASis), which evaluates antibody humanness based on peptide search in natural antibody repertoires and germline sequence identity.

While existing humanization tools have significantly advanced the development of therapeutic antibodies, amino acid modifications can potentially lead to immunogenicity, as well as affect the structural integrity and binding affinity of the antibody. Molecular dynamics (MD) simulations offers an in-depth understanding of the dynamic behavior and stability of antibodies at an atomic level, which is vital for comprehending antibody-antigen interactions and overall stability. [15] This method is particularly valuable for assessing the impact of modifications, such as CDR grafting and back mutations, on the structural and functional integrity of antibodies. [16,17] Additionally, MD simulations was employed to obtain valuable insights into the structural alterations resulting from residues mutations in the affinity-enhanced HuScFv. [18]

CD99, a glycosylated transmembrane protein, is integral to processes such as cell adhesion, migration, and differentiation. [19,20] However, its dysregulation has been linked to the development and progression of several T-cell malignancies. [21] While fully human anti-CD99 antibodies have been developed and tested in various formats (e.g., single-chain variable fragment (ScFv), diabodies, and full-length antibodies), [22,23] the humanization of murine antibodies remains a relevant challenge due to their unique binding properties and therapeutic potential. The mouse anti-CD99 monoclonal antibody (MT99/3) demonstrated T cell proliferation inhibition and the ability to enhance immune effector functions. [24,25] Despite these promising properties, the therapeutic application of full monoclonal antibodies is constrained by their immunogenicity. Recently, HuScFvMT99/3, a humanized single-chain variable fragment (HuScFv) against CD99, was engineered. This construct exhibited binding activity comparable to the full monoclonal antibody and preserved the binding region to CD99 at VDGENDDPRPP (residues 60–70), similar to MT99/3. [26] However, CDR grafting of mouse antibodies onto human frameworks demonstrates a high risk of immunogenicity, necessitating improvements in the humanness property of HuScFvMT99/3.

AlphaFold (AF) has revolutionized antibody design by providing reliable structural models that were previously challenging to access. This tool has accurately generated over 400 antibody-antigen complex structures with improved near-native modeling. [27] Furthermore, AlphaFold2 (AF2) has proven instrumental in facilitating the humanization of the anti-PD-L1 antibody h3D5-hIgG1, highlighting its potential in advancing therapeutic antibody development. [28] This study focuses on the impact of BioPhi-guided humanness improvements on the binding affinity of HuScFvMT99/3 to CD99. Various humanness evaluation methods and PITHA were employed to assess the humanness and immunogenicity of HuScFvMT99/3 variants. AF2 [29] was applied to predict the structural interactions between HuScFvMT99/3, along with its humanized variants, and the CD99 peptide epitope. MD simulation was conducted to assess the dynamic behavior of the predicted structure.

To ensure consistency in structure prediction, alternative modeling methods, AlphaFold3 (AF3) [30] and HADDOCK (HD) [31] were utilized alongside AF2. The $\Delta G_{binding}$ and per-residue decomposition energy were calculated to understand the energetic contributions to binding affinity. Furthermore, principal component analysis (PCA) was performed to evaluate the conformational dynamics of the complexes. The binding characteristics of HuScFvMT99/3 variants were validated using enzyme-linked immunosorbent assay (ELISA) and biolayer interferometry (BLI). Binding activity against surface CD99 on Jurkat cells was further assessed by flow cytometry. By integrating computational predictions with experimental validation, this study provides a comprehensive framework for designing humanized antibodies, advancing the development of therapeutic antibodies for future applications.

2. Materials and methods

2.1. Humanization and structural model prediction of HuScFvMT99/3 variants

The amino acid sequence of the wild-type (WT) HuScFvMT99/3 (HuScFvMT99/3^{WT}) was introduced to BioPhi software [14] to improve the humanness through substitution of amino acids at framework regions. The variable region sequence of antibodies was numbered using the Kabat numbering system. The improved HuScFvMT99/3 is called HuScFvMT99/3^{BP}. Additionally, a hybrid version, HuScFvMT99/3^{HY}, was designed by combining the light chain variable region from HuScFvMT99/3^{WT} (VL^{WT}) with the heavy chain variable region from HuScFvMT99/3^{BP} (VH^{BP}). Humanness scores for each variant were calculated using T20 score [12] and SAbPred [13] analysis software.

The predicted structure of HuScFvMT99/3^{WT} and its variants (HuScFvMT99/3^{BP} and HuScFvMT99/3^{HY}) was generated using AF2 (Fig. 1). [29,32] The structural similarity of HuScFvMT99/3 variants was determined through pairwise structural alignment and estimated RMSD analysis using the RCSB PDB server. [33] The specific determining residues (SDRs) on VH and VL of HuScFvMT99/3 variants were indicated by Prodigy. [34,35] The structural complex of each variant was submitted to the PITHA web server [36] to estimate the cavity volume at the CDR region, the hydrophobicity at the CDR-H3 loop, and predicted immunogenicity.

2.2. Computational calculations

2.2.1. Model variants and structure preparation

The complex structure of each HuScFvMT99/3 variant with or without CD99 peptide (residues: 60VDGENDDPRPP70) was obtained from AF2. [29] To prepare the structure for the MD simulations, each complex system under periodic boundary conditions was solvated in a cubic box of TIP3P water model extending to 10 Å along each direction from the complex model with counter ions added to neutralize the

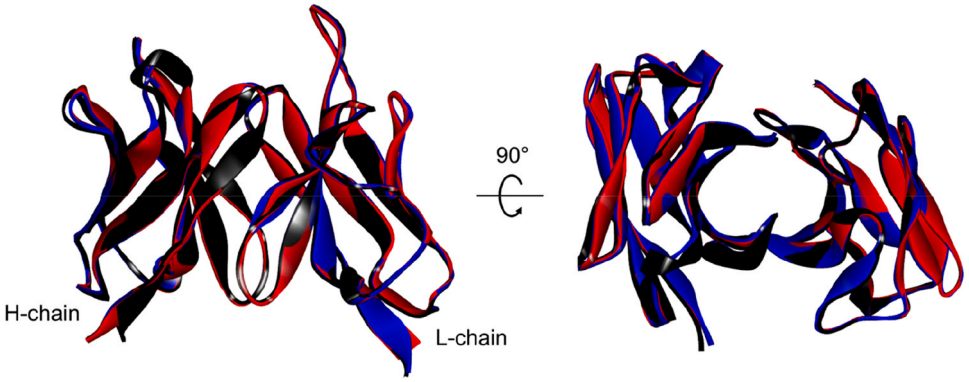

Fig. 1. Structure alignment of HuMT99/3 variants. Comparative ribbon structure of HuScFvMT99/3^{WT} (black), HuScFvMT99/3^{BP} (red) and HuScFvMT99/3^{HY} (blue) was generated by AF2. The conformational structure of HuScFvMT99/3 variants was compared using Chimera software version 1.18. Analysis by the RCSB PDB server showed RMSD of 0.66 and 0.64 Å for VH and 0.19 and 0.17 Å for VH of HuScFvMT99/3^{BP} and HuScFvMT99/3^{HY}, respectively.

system. The LeaP module embedded in AMBER 22 software [37] was used for adding the missing atoms with the FF14SB force field [38] for applying the description of the protein characterization. The cut-off distance keeps to 12 Å to compute the non-bonded interactions. Particle-mesh Ewald (PME) method was used for calculating the long-range electrostatic interactions. SHAKE algorithm was applied to constrain the bonds that involved hydrogen atoms.

The CUDA-based program from the AMBER 22 program was used by PMEMD.CUDA module. [39,40] for speeding up the simulation times. Each system was first minimized using the steepest descent protocol followed by a conjugate gradient procedure for relaxation and elimination of overlapping atoms. The first step was to allow, out of 10,000 iterations, only water molecules to move. In the second step, in each of the 10,000 iterations, hydrogen and protein side chains were relaxed, in a fixed order. Finally, 20,000 steps were calculated with the restriction-free system. After energy minimization, the optimized MD systems were conducted gradually by heating (H) phase NVT (constant number of atoms, volume, and temperature) ensemble with the fixed protein atoms for 100 ps from 0 to 310.15 K (37°C) by using a force constant of 10 kcal mol^{-1} Å^{-2}. This was followed by 1000 ps of equilibration (Eq1) phase NVT-MD at 310.15 K at a force constant of 5.0 kcal mol^{-1} A^{-2}. Then, 10,000 ps without any constrained forces of equilibration-2 (Eq2) phase NPT-MD were performed for each fully flexible equilibrium system at the same temperature and one atm pressure. The density of each system was about 1.0 g cm^3. Finally, 100 ns of unrestrained production (Prod) phase NVT-MD simulation were applied at a constant temperature of 310.15 K. The time step of 2 fs was set, and the trajectory was recorded every 0.2 ps. Structural analysis of the RMSD, the root-mean-square fluctuation (RMSF), and the principle component analysis (PCA) were carried out by CPPTRAJ module [41] using the Amber 22 program. The structural images were presented using DS software.

2.2.2. Binding free energy and per-residue decomposition energy analysis

Amber molecular mechanics Poisson–Boltzmann surface area (MM-PBSA) [42] method was applied to estimate the binding free energy ($\Delta G_{binding}$, kcal mol^{-1}) of the complex using the snapshot structures extracted from the last 30 ns (total 15,000 snapshots) Prod-phase trajectory data. The binding free energy ($\Delta G_{binding}$, kcal mol^{-1}) and per-residue decomposition energy (ΔG_{decomp}, kcal mol^{-1}) were calculated for each variant species in the energetic framework of the MM-PBSA method, and the binding free energy was computed from the following equation:

$$\Delta G_{binding} = \Delta G_{Complex} - (\Delta G_{HuScFvMT99/3} + \Delta G_{CD99}) = (\Delta E_{vdW} + \Delta E_{EEL} + \Delta G_{Solvation}) - T\Delta S \quad (1)$$

In which ΔE_{vdW} and ΔE_{EEL} refer to the van der Waals and electrostatic contribution calculated by the molecular mechanics force field, and $\Delta G_{solvation}$ represents the solvation-free energy. The entropy changes of the protein-protein complex ($-T\Delta S$, kcal mol^{-1}) were calculated using the normal mode analysis of the vibrational frequencies.

2.2.3. Principal component analysis (PCA)

To evaluate the displacement of atoms and conformational dynamics of a protein complex, PCA was performed and analyzed using a covariance-matrix-based approach. [43–45] The elements of the positional covariance matrix C were obtained based on the following Eq. 2:

$$C_{ij} = \langle (x_i - \langle x_i \rangle) \times (x_j - \langle x_j \rangle) \rangle \quad (2)$$

Here x_i and x_j represent the instantaneous coordinates of the i^{th} and j^{th} Cα-atoms of the system, used to construct matrix C, while $\langle x_i \rangle$ and $\langle x_j \rangle$ denote ensemble averages. The averaged values are computed over the Prod-MD simulations after superimposition on a reference structure using the CPPTRAJ module of the AMBER 22, solvent water molecules and neutralizing ions added by the Leap module are stripped prior to MD trajectory generation. PCA was performed for Cα-atoms on 15,000 snapshots each. PC1 and PC2, which represent the first two principal components, are created from the trajectories averaged from the WT and the variant systems. The trajectories were analyzed for the relative motions about their center of masses.

2.3. Production and binding activity characterization of HuScFvT99/3 variants

2.3.1. Production and purification of HuScFvMT99/3 variants

The plasmid pET-21a-*HuScFvMT99/3^{BP}* (*His6X*) and pET-21a-*HuScFvMT99/3^{HY}* (*His6X*) were synthesized for protein expression in *Escherichia coli* (*E. coli*) system. The plasmids construction was depicted in Fig. 2. The HuScFvMT99/3 construct was designed with the VL-$(G_4S)_3$-VH configuration to facilitate proper folding and stability, as reported in previous studies. [46] This flexible linker helps maintain the relative orientation of the variable domains, minimizing steric hindrance and ensuring functional binding. Additionally, the HuScFvMT99/3 genes were flanked with a C-terminus histidine tag, which facilitates protein purification. The genes were inserted into pET-21a (+) plasmid at *Nde*I and *Xho*I restriction sites.

The plasmids, including pET-21a-*HuScFvMT99/3^{WT}* (*His6X*) [26], pET-21a-*HuScFvMT99/3^{BP}* (*His6X*) and pET-21a-*HuScFvMT99/3^{HY}* (*His6X*), were transformed into *E. coli* Origami B (DE3) competent cells for recombinant HuScFvMT99/3^{WT}, HuScFvMT99/3^{BP} and HuScFvMT99/3^{HY} production, respectively. A single colony was picked and inoculated in super broth (SB) supplemented with 100 μg/mL of ampicillin, 15 μg/mL of kanamycin, 12.5 μg/mL of tetracycline, and 0.05 % of glucose. The bacterial culture was incubated at 37C with 200 rpm

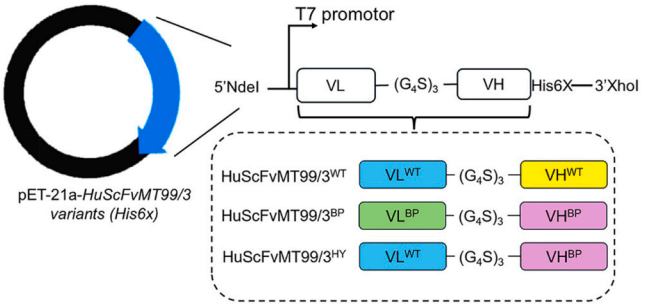

Fig. 2. Schematic of HuScFvMT99/3 variants encoding plasmids. The pET-21a plasmid harbors the gene encoding HuScFvMT99/3^{WT}, HuScFvMT99/3^{BP} and HuScFvMT99/3^{HY}. The VL and VH domains of HuScFVMT99/3 constructs were linked together with $(G_4S)_3$ linker. The HuScFvMT99/3 variants gene was flanked with a C-terminus histidine tag. VL^{WT} and VL^{BP} indicate the VL domain of HuScFvMT99/3^{WT} and HuScFvMT99/3^{BP}, respectively. VH^{WT} and VH^{BP} indicate the VH domain of HuScFvMT99/3^{WT} and HuScFvMT99/3^{BP}, respectively.

swirling until an optical density (OD) at 600 nm reached 0.8–1. The 0.5 mM of IPTG was added to the bacterial culture to induce protein expression, and this process continued at 20℃ for 16–18 h. After incubation, bacterial cells were pelleted and washed three times with phosphate-buffered saline (PBS). The bacterial cell was lysed via three sonication times of 5 min each at 0.5 cycles with 80 % amplitude on ice, followed by centrifugation at 4000 ×g for 30 min at 4 °C. The lysate was collected and subjected to a purification process by affinity chromatography using Ni-NTA agarose (QIAGEN, 30210).

The purified HuScFvMT99/3^{WT} (His6X), HuScFvMT99/3^{BP} (His6X), and HuScFvMT99/3^{HY}(His6X) were separated by 15 % sodium dodecyl sulfate-polyacrylamide gel electrophoresis (SDS-PAGE) to determine the purity of the protein. Proteins were transferred onto a nitrocellulose membrane and subsequently probed with 1:3000 dilution of HRP-conjugated anti-His antibody (Biolegend, 652504). The reaction was developed using a LumiGLO® Peroxidase Chemiluminescent Substrate Kit (Sera care, 54300042). The molecular estimation relies on Precision Plus Protein™ Kaleidoscope™ Prestained Protein Standards (BioRad, 610375).

2.3.2. Binding activity assessment of HuScFvMT99/3 variants using ELISA

The binding activity of HuScFvMT99/3^{WT} (His6X), HuScFvMT99/3^{BP} (His6X) and HuScFvMT99/3^{HY} (His6X) against the CD99 epitope was determined using ELISA. Microwells were coated with 10 μg/mL of avidin at 37℃ for overnight. The avidin-coated wells were washed with 0.05 % tween in PBS (washing buffer), followed by adding 2 % bovine serum albumin (BSA) in PBS (blocking solution). The reaction was incubated at 37℃ for 1 h. After washing step, the biotinylated CD99 peptide target epitope (Biotin-Ahx-AVVDGENDDPRPPNP) [26] at 2 μg/mL was added to the wells and incubated at 37℃ for 1 h. After incubation, the wells were washed three times with washing buffer, then incubated with 1 or 5 μg/mL of HuScFvMT99/3 variants at 37℃ for 1 h. The well without HuScFvMT99/3 served as a no-ScFv control. After washing, 1:3000 dilution of HRP-conjugated anti-His antibody was added to the reaction. The reaction was developed by adding TMB chromogen substrate (Sera care, 5120–0076) and was quenched by 1 N HCl solution. The OD at 450 nm was read using a microplate reader.

2.3.3. Binding affinity determination of HuScFvMT99/3 variants using Biolayer Interferometry (BLI)

To assess the binding affinity of HuScFvMT99/3 variants, the BLI technique was employed. The binding kinetic was evaluated using the Octet® K2 instrument (ForeteBio). All of the analysis steps were conducted in assay buffer (2 % BSA in 0.05 % Tween 20 in PBS) at 30°C. Biotinylated CD99 peptide was immobilized onto the surface of the streptavidin biosensor tip at 10 μg/mL. Next, the biosensors were washed with the assay buffer. The pre-immobilized biosensors were immersed in solutions of HuScFvMT99/3 variants at various concentrations to initiate the association phase. The dissociation phase was monitored by immersing biosensors into the assay buffer. The fitting curves were analyzed using 1:1 fitting mode by Octet software. The equilibrium constant (K_D) was calculated from the ratio K_{off}/K_{on}.

2.3.4. Cell line

Jurkat T cells clone E6.1 (ATCC) were cultured in Roswell Park Memorial Institute (RPMI) medium (Gibco, 31800105) supplemented with 10 % heat-inactivated fetal bovine serum (HI-FBS) (Gibco, 5256701), 100 U/mL of penicillin, 100 μg/mL of streptomycin (Gibco, 15140122), and 2 mM of L-glutamine (Gibco, 25030081) (C-RPMI).

2.3.5. Binding activity determination of HuScFvMT99/3 variants against CD99 on Jurkat T cell using flow cytometry

Immunofluorescence staining was used to determine the binding activity of HuScFvMT99/3 variants against surface CD99 on Jurkat T cells. 5×10^5 of Jurkat T cells were incubated in 10 % heat-inactivated human AB serum in PBS to block the Fc receptor. After blocking, 20 μg/mL of HuScFvMT99/3 variants were added to blocked cells. Cells were incubated on ice for 30 min, then washed twice with a FACs diluent (2 % FBS-0.5 mM EDTA, 0.1 % NaN_3 in PBS). The condition without HuScFv, a conjugate control, served as the negative control for this experiment. After washing, cells were incubated with a 1:10 dilution of PE-conjugated anti-His tag antibody (Biolegend, 362603). The stained cells were washed three times with a FACs diluent and resuspended in 1 % paraformaldehyde in PBS. The percentage of CD99 positive cells and mean fluorescence intensity were analyzed by flow cytometry using BD Accuri™ C6 plus (BD biosciences).

Inhibition immunofluorescence staining was also performed to ensure the binding activity of HuScFvMT99/3 variants against CD99 on Jurkat T cells. HuScFvMT99/3 variants at 20 μg/mL were pre-incubated with 50 μg/mL of CD99 peptide prior to being added to Jurkat T cells. The reaction was incubated on ice for 30 min. The condition lacking HuScFv; a conjugate control, served as a negative control for this experiment. Cells were washed three times with a FACs diluent, followed by incubating with 1:10 dilution of PE-conjugated anti-His tag antibody. The stained cells were washed three times with a FACs diluent and resuspended in 1 % paraformaldehyde in PBS. The percentage of CD99-positive cells was analyzed by flow cytometry using BD Accuri™ C6 plus. The percentage of inhibition (% inhibition) was calculated by [(MFI of uninhibited) ÷ (MFI of inhibited)] × 100.

2.3.6. Statistical analysis

Data were expressed as mean ± SD from triplicate experiments. One-way ANOVA was used for comparison. $p \leq 0.05$ was considered statistically significant.

3. Results

3.1. Humanization, humanness scores calculation, and immunogenicity prediction of HuScFvMT99/3 variants

To enhance the humanness of HuScFvMT99/3, the amino acid sequences of the VH and VL domains of HuScFvMT99/3^{WT} were submitted to BioPhi. The amino acid modifications suggested by BioPhi are highlighted in red, excluding CDRs (Fig. 3). HuScFvMT99/3^{BP} showed a slight increase in the humanness score for the VL domain, while a significant improvement was observed in the VH domain (Table 1). The humanness scores of HuScFvMT99/3^{WT} and its variants were also evaluated using the T20 score analyzer and SAbPred analysis. The VL domain of HuScFvMT99/3^{BP} exhibited a decrease in the humanness score according to the T20 score analyzer, while SAbPred classified it as "not human". Consequently, HuScFvMT99/3^{HY} was designed by

Fig. 3. Amino acid sequence of HuScFvMT99/3 variants. The sequence of (A) VH and (B) VL domains of HuScFvMT99/3 variants were aligned. The red letter indicates a modified amino acid in the sequence. The CDRs of VH (CDR-H1–3) and VL (CDR-L1–3) identification as listed in bold letters relied on Kabat's numbering rule. The specific determining residues (SDRs) on HuScFvMT99/3 variants were identified using Prodigy as highlighted in yellow color.

Table 1
Humanness scores calculation of HuScFvMT99/3 variants. The humanness scores of VH and VL domain of HuScFVMT99/3 variants were calculated by humanness score evaluation software including BioPhi, T20 cores and SAbPred analysis.

	Humanness scores					
	BioPhi		T20 score		SAbPred	
	VL	VH	VL	VH	VL	VH
HuScFvMT99/3^{WT}	87 % identity		94.74		0.74	
HuScFvMT99/3^{BP}	88 % identity		88.16		Not human	
HuScFvMT99/3^{HY}	87 % identity		94.74		0.74	
HuScFvMT99/3^{WT}		64 % identity		80.74		0.73
HuScFvMT99/3^{BP}		77 % identity		87.47		0.85
HuScFvMT99/3^{HY}		77 % identity		87.47		0.85

Table 2
Immunogenicity prediction of HuScFvMT99/3. The structural complexes of all HuScFvMT99/3 variants were analyzed for immunogenicity using PITHA. The predicted data, including cavity volume in the CDR region, hydrophobicity at the CDR-H3 loop, and predicted immunogenicity, are presented.

Antibody	Cavity volume at the CDR region (Å^3)	Hydrophobicity at CDR-H3 loop (Å^2)	Immunogenicity prediction
HuScFvMT99/3^{WT}	0	146.5	High
HuScFvMT99/3^{BP}	520.8	137.1	High
HuScFvMT99/3^{HY}	664.1	137.5	High

combining VL^{WT} with VH^{BP} to preserve its humanness.

As seen in Fig. 1, RMSD analysis of the predicted HuScFvMT99/3 variants structure was calculated by the RCSB PDB server. The RMSD values were 0.66 Å and 0.64 Å for VH, and 0.19 Å and 0.17 Å for VL in HuScFvMT99/3^{BP} and HuScFvMT99/3^{HY}, respectively. RMSD analysis indicated high structural similarity in the VL domain of HuScFvMT99/3^{WT} and its variants, while the VH domain showed slightly lower similarity.

Additionally, PITHA was utilized to predict the immunogenicity of HuScFvMT99/3 and its variants. The results indicated that HuScFvMT99/3^{WT} was predicted to exhibit high immunogenicity (Table 2). Notably, the cavity volumes of HuScFvMT99/3^{BP} and HuScFvMT99/3^{HY} were greater than that of HuScFvMT99/3^{WT}, measuring 520.8 Å^3 and 664.1 Å^3 , respectively. However, there was no significant difference in hydrophobicity at the CDR-H3 loop.

3.2. MD simulations

3.2.1. Structural analysis, stability, and flexibility of HuScFvMT99/3 variants

The 3D structures of the HuScFvMT99/3^{WT} (VH-VL domains) and its variant (HuScFvMT99/3^{BP}, and HuScFvMT99/3^{HY}), modeled using AF2 [27], were subjected to the MD simulations calculations. Various structural analysis was performed to study the structural impact of each system. Comprehensive structural analyses were performed to evaluate the structural impact of each system. To assess the dynamics and stability of the ScFv variants, the RMSD relative to the optimized complex structure was monitored throughout the entire MD simulation trajectory, as depicted in Fig. 4. The RMSD plot showed steady oscillations and minimal fluctuations for each complex model compared to HuScFvMT99/3^{WT} (Fig. 4A). The RMSD plot of the HuScFvMT99/3^{WT} system was found to be slightly higher as compared with the values for the observed variants, indicating the higher flexibility and/or significant conformational changes in the VH-VL domains. In contrast, the HuScFvMT99/3^{BP} showed stable RMSD with inconsiderable fluctuations and endured lesser conformational changes during the whole MD simulations, suggesting the VH-VL domains maintain their native fold with good stability. A slight conformational shift was observed in the HuScFvMT99/3^{HY} at around 85 ns, which later stabilized, suggesting adaptive conformational changes due to the use of the VL^{WT}.

Fig. 4B shows the RMSD distribution over the MD simulations. The lower RMSD distribution in both HuScFvMT99/3^{BP} (0.975 Å) and HuScFvMT99/3^{HY} (1.075 Å) suggests greater stability compared to the HuScFvMT99/3^{WT} (1.225 Å). In addition, the HuScFvMT99/3^{HY} showed a slightly broader distribution (~0.9 Å) compared to the other systems (~0.8 Å in both HuScFvMT99/3^{WT} and HuScFvMT99/3^{BP}). Although this difference is not significant, the VH-VL domains of

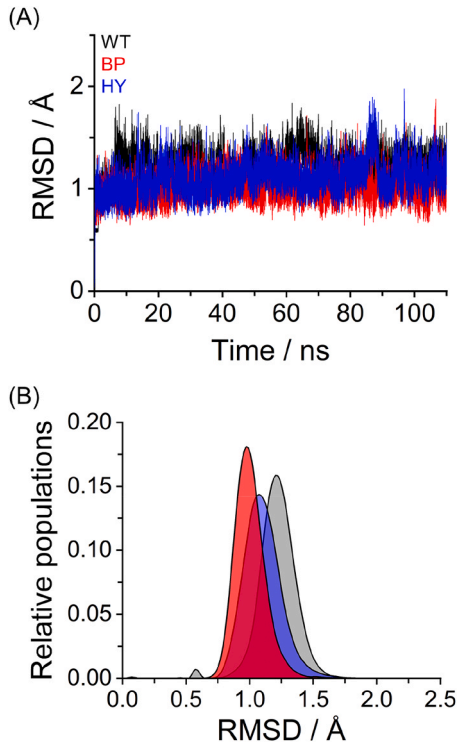

Fig. 4. Comparison of RMSD for HuScFvMT99/3; WT (black), BP (red), and HY (blue) analyzed during prod-phase MD simulations. (A) RMSD plot, and (B) RMSD distribution of Cα-atom of HuScFvMT99/3 VH-VL domain.

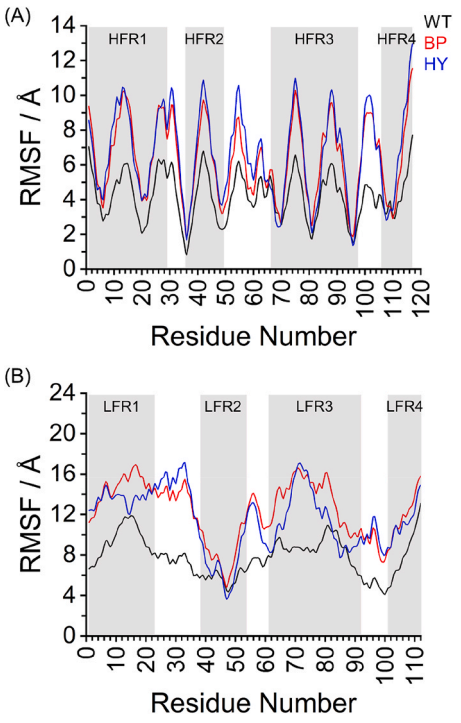

Fig. 5. Comparison of RMSF for HuScFvMT99/3; WT (black), BP (red), and HY (blue) analyzed during prod-phase MD simulations. (A) RMSF of ScFv H-chain. and (B) RMSF of ScFv L-chain. The residues in FR in H-chain and L-chain, are highlighted in grey squares.

HuScFvMT99/3^{HY} may undergo substantial conformational fluctuations during the simulation.

To gain a deeper understanding of the structural properties of the potential models, we assessed the structural flexibility of the protein-protein complexes throughout the experimental simulation of the HuScFvMT99/3 variants. Specifically, we analyzed the dynamics of the residues by calculating the RMSF over the last 30 ns of the production phase of the MD simulations. This approach provides valuable insight into the flexibility and/or rigidity of protein-protein interactions. As shown in Fig. 5, the RMSF plots revealed similar fluctuation patterns with different magnitudes, particularly within the FR of both the H-chain and L-chain across the variants. The HuScFvMT99/3 variants (BP and HY), which share the same heavy chain variable region, exhibited greater fluctuations, indicating higher flexibility or structural mobility in these variants compared to the WT. Consequently, the less stable HuScFvMT99/3 variants showed deviations from the humanness score, especially in the heavy chain, when compared to the WT. In contrast, the WT displayed the lowest fluctuations in the amino acid residues, suggesting enhanced stability, which may reflect a more stable interaction with the binding partner.

Focusing on the light chain variable region of each variant (Fig. 5B), only a structural adjustment in HuScFvMT99/3^{BP} was necessary to stabilize the binding surface configuration. In contrast, HuScFvMT99/3^{HY}, designed with VL^{WT}, exhibited additional instability in the VH-VL domain. While the RMSF value for the light chain in HuScFvMT99/3^{HY} remained comparable to the WT, certain amino acid positions in the framework region, as predicted by BioPhi (highlighted in red in Fig. 3), were constrained to align with the WT. This suggests that structural adjustments in the light chain variable region of HuScFvMT99/3^{HY}, particularly involving key amino acids, are essential for maintaining ScFv binding stability, leading to reduced fluctuations in the framework region.

Since the biological function of a protein-protein interaction is influenced by its conformational dynamics, a detailed analysis of these dynamics is essential. In this study, we employed PCA, a robust method for extracting and interpreting the dominant motions and conformational dynamics of proteins. This was accomplished by diagonalizing the covariance matrix of Cα–atom fluctuations during the production phase of the MD simulations. Fig. S1 illustrates the PCA scatter plot for the VH-VL domains of HuScFvMT99/3WT and its variants, along the first two principal components (PCs). The results revealed that both HuScFvMT99/3 variants (BP and HY) occupied a broader region of the conformational space compared to HuScFvMT99/3^{WT}. This suggests that the variants exhibit greater flexibility and conformational variability, implying higher mobility or potential structural instability in the VH-VL domain relative to the WT. In contrast, the tight clustering of HuScFvMT99/3^{WT} indicates limited structural flexibility, maintaining a more rigid conformation with fewer dynamic rearrangements in the VH-VL domain. This rigidity may contribute to a more consistent molecular movement.

3.2.2. Energetic and structural affinities of HuScFvMT99/3 CD99 binding complexes

To investigate the conformational changes associated with the energetic affinities of protein-protein interactions, the predicted complex structures of HuScFvMT99/3 and the CD99 peptide were preliminarily modeled using the AF2 method modeled. [29] Then, the 100 ns long-time of the MD simulations of complexed HuScFvMT99/3 binding to CD99 were performed. According to the thus-obtained predicted complexes, we found that the docked structure of the CD99 peptide preserves the same binding interface information. A key feature in the docked complexes was the interaction of hydrophilic residues at the CDR binding sites of HuScFvMT99/3, which was conserved throughout the MD simulations (Fig. S2). Table 3 presents the $\Delta G_{binding}$ values, initially analyzed during the production phase of MD simulations using molecular mechanics calculations via the MM-PBSA method.

Comparing with the complexed HuScFvMT99/3^{WT} (–9.56 kcal mol^{-1}), the variant species of complexed HuScFvMT99/3^{BP}

Table 3
Energy component (kcal mol^{-1}) of HuScFvMT99/3 variants binding to CD99 protein estimated by MM-PBSA method.

Parameter	HuScFvMT99/3^{WT}			HuScFvMT99/3^{BP}			HuScFvMT99/3^{HY}		
	AF2	AF3	HD	AF2	AF3	HD	AF2	AF3	HADDOCK
$\Delta G_{binding}$	**–9.59 ± 10.170**	**–15.58 ± 17.763**	**–21.17 ± 9.492**	**–28.90 ± 9.759**	**4.23 ± 8.702**	**6.15 ± 7.814**	**–24.78 ± 10.281**	**–12.78 ± 15.277**	**–13.03 ± 9.608**
vdW	–49.88 ± 4.968	–46.96 ± 5.038	–60.62 ± 5.745	–56.59 ± 5.974	–47.58 ± 5.442	–26.30 ± 7.146	–46.14 ± 5.128	–43.91 ± 5.435	–51.89 ± 4.806
EEL	–471.00 ± 42.297	–525.08 ± 62.813	–611.92 ± 52.147	–472.30 ± 41.625	–323.04 ± 37.489	–335.78 ± 25.956	–534.68 ± 34.919	–512.22 ± 57.282	–522.22 ± 40.043
EPS	477.12 ± 41.219	522.91 ± 48.362	609.41 ± 48.912	464.46 ± 35.496	339.99 ± 38.877	342.28 ± 26.195	524.20 ± 32.708	510.01 ± 15.931	525.91 ± 34.812
ENPOLAR	–43.40 ± 2.201	–38.91 ± 2.951	–50.22 ± 3.777	–49.73 ± 2.291	–35.28 ± 3.936	–24.67 ± 5.033	–42.93 ± 2.373	–37.83 ± 2.718	–44.89 ± 2.163

Note: The EEL and vdW represent the electrostatic and van der Waals contributions from MM, respectively. EPS stands for PB electrostatic contribution to the polar solvation-free energy, while ENPOLAR is the nonpolar contribution to the solvation-free energy. $\Delta G_{binding}$ (kcal mol^{-1}) is the final estimated binding free energy calculated from the terms above.

($\Delta G_{binding}$ = –28.90 kcal mol^{-1}) and complexed HuScFvMT99/3^{HY} (–24.78 kcal mol^{-1}) showed a significantly stronger affinity to the CD99 peptide. Although the HuScFvMT99/3^{WT} VH-VL shows a stable and compact structure with low mobility, these features do not enhance the affinity of the docked CD99 peptide at the CDR binding interface. As expected, the complex variants of HuScFvMT99/3^{BP} and HuScFvMT99/3^{HY} had a positive impact on the complex stability with a negative $\Delta G_{binding}$ value that is due to the decreasing of the vdW and EEL terms, respectively, in respect to the WT system (Table 3). In the later section, we will discuss the structural analysis of the complexed proteins by considering the conservative character in the flexibility and stability between ScFv VH-VL domain and the peptide.

As mentioned above, the structural complexes of HuScFvMT99/3 variants and the CD99 peptide were also modeled using alternative methods, such as AF3 [30] and HD. [31] As shown in Table 3 and Fig. 6, the AF3 and HD methods rarely agreed with the AF2 predictions, both in terms of structural key hotspots and the confidence of binding affinities. The $\Delta G_{binding}$ value indicated that the HuScFvMT99/3^{WT} complex, obtained from AF3 and HD prediction methods, significantly exhibited the strongest affinity for the CD99 epitope, while the HuScFvMT99/3^{BP} complex showed the weakest. The $\Delta G_{binding}$ value of the HuScFvMT99/3^{WT} complex improved, suggesting better binding affinity. In contrast to, the complexed HuScFvMT99/3^{HY}-CD99 model exhibits greater binding affinity than the HuScFvMT99/3^{BP} CD99 model likely due to the merging of the VL^{WT} and VH^{BP} domains.

To better understand these results, the binding free energies were decomposed into the energy contributions of the individual residues at the binding interface. This approach aims to provide insights into the cross-reactivity of the neutralizing antibody response. Fig. 7 illustrates the comparison alternative modelling methods, AF2, AF3, and HD, of the decomposed per-residue free energy (ΔG_{decomp}, kcal mol^{-1}) of the complexed HuScFvMT99/3 CDRs regions (VH and VL domains) with CD99 epitope calculated by the MM-PBSA method. Negative values represent favorable interactions, while positive values indicate unfavorable contributions. The final MD structures of each variant system related to the key hotspots at the binding interface (Fig. 7) are illustrated in Figs. 8–10. As shown in Fig. 7, the predictive models of the AF2 method showed the key residues in the VH-VL domain of HuScFvMT99/3 CDRs differ from the other AF3 and HD methods. The mutated FW regions (BP and HY) quite affect the highlighted hotspots favorable interactions at the CDRs binding interfaces compared with the HuScFvMT99/3^{WT}-CD99 complex. Considering the WT model in each predictive method, the complex CD99-HuScFvMT99/3^{WT} highlighted the significant potential residues on the CDR VH domain for CD99 binding, especially the predicted complex from the HD method. As a result, the R50 position of the VH domain showed high potential individual decomposed energy for all complex systems.

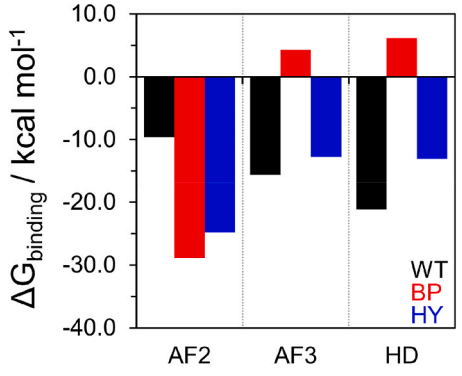

Fig. 6. Comparison of alternative modelling methods, AF2, AF3, and HADDOCK (HD), of the binding free energy ($\Delta G_{binding}$, kcal mol^{-1}) for HuScFvMT99/3 CD99 complexes. The complexed HuScFvMT99/3 CD99 in WT (black), BP (red), and HY (blue) were analyzed during the prod-phase MD simulations.

Comparing all predictive modelling methods, the strong per-residue interaction in the CDR-H domain in all variants contributed to the tighter binding of HuScFvMT99/3 to the CD99 epitope. However, in the AF2 modelling, the key CDR positions contributed less to the interaction in the HuScFvMT99/3^{WT} than those of the variant systems, leading to the weaker affinity of the WT complex. In contrast, the decomposed energy values from AF2, AF3, and HD methods did not show significant differences in the favorable contact with CD99 at the CDR VL domain for each HuScFvMT99/3 system. This suggests that mutations in the framework regions have a greater impact on the binding activity of the CDR loops in the VH domain than in the VL domain of HuScFvMT99/3 when binding to the CD99 epitope.

3.2.3. Structural analysis and stability of HuScFvMT99/3 CD99 binding complexes

To further investigate the unstable structure of the HuScFvMT99/3-CD99 binding complexes, PCA was employed to explore the conformational transitions of both the unbound systems and the HuScFvMT99/3-CD99 complex during MD simulations, as shown in Fig. 11. The PCA scatterplots for the HuScFvMT99/3-CD99 complexes, generated across the predictive modelling methods (AF2 in green, AF3 in blue, and HD in red), revealed significant differences between the complexes along the direction of PC1 and PC2.

As discussed earlier, excessive variability can weaken binding interactions. It was observed that the HD-modeled complexes of HuScFvMT99/3^{WT} and HuScFvMT99/3^{HY} exhibited lower conformational diversity (ranging from −10–10) compared to the HuScFvMT99/3^{BP} complex (ranging from −20–25). This indicates stronger binding affinities for the former, due to reduced structural mobility during the

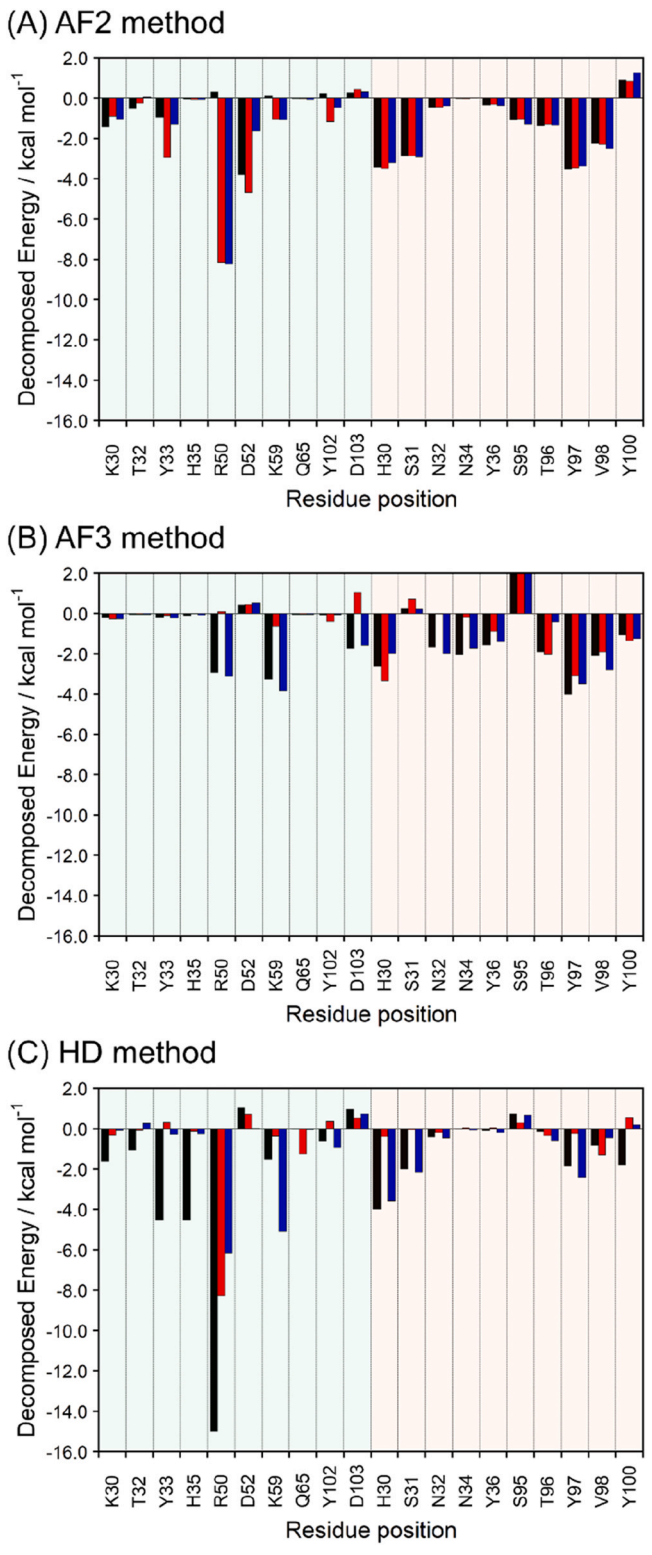

Fig. 7. Per residue free energy decomposition of HuScFvMT99/3 complex with CD99 peptide predicted models by AF2, AF3, and HD methods. The key residues in CDRs VH (green) and VL (orange) domains with the total binding free energy (ETOT) components are presented in each variant of the HuScFvMT99/3 CD99 complex. WT (black), BP (red), and HY (blue).

simulations. A similar trend was observed for the HuScFvMT99/3-CD99 complexes predicted using the AF3 method. The HuScFvMT99/3^{BP}-CD99 complex, obtained from both the AF3 and HD methods, displayed a broader conformational space compared to the AF2 model. This

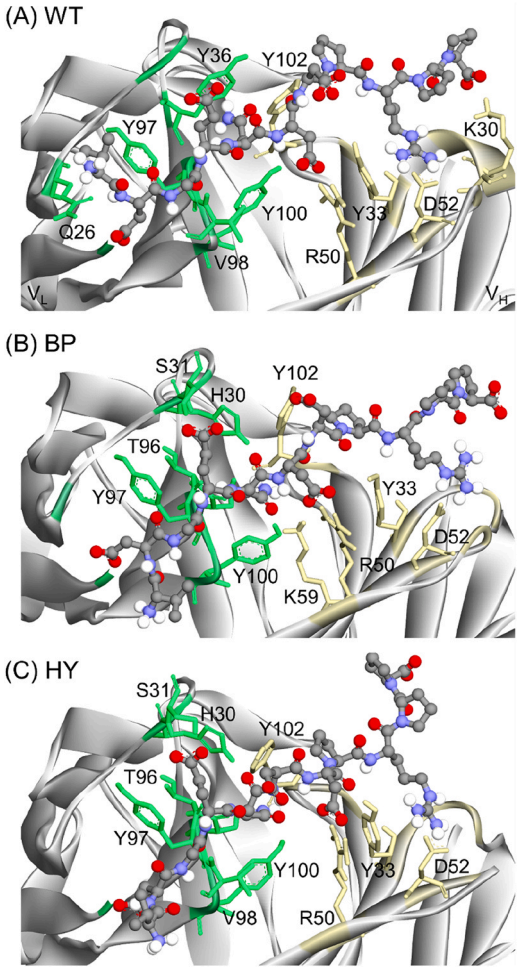

Fig. 8. Structural mapping of the binding interface obtained from the Prod phase MD simulations between HuScFvMT99/3, (A) WT, (B) BP, and (C) HY models, complex with CD99 peptide predicted models by AF2 method. The secondary structures of VH-VL domains and CD99 peptide are portrayed as white ribbons and ball-stick style, respectively. The interfacial residues of ScFv are annotated and shown in yellow (VH) and green (VL) sticks. Each interacting amino acid residue is highlighted in black-color labeled. The figure was drawn by Discovery Studio 2019 Client (Biovia software).

implied that the CD99 peptide enhances structural flexibility at the binding interface of HuScFvMT99/3^{BP}. Notably, the AF2-modeled HuScFvMT99/3-CD99 complex exhibited greater conformational variability during the simulations, except when complexed with HuScFvMT99/3^{BP}, where slight stabilization was observed, leading to a narrower conformational range.

3.3. Construction and production of HuScFvMT99/3 variants

The pET-21a-*HuScFvMT99/3^{WT} (His6X)*, pET-21a-*HuScFvMT99/3^{BP} (His6X)* or pET-21a-*HuScFvMT99/3^{HY} (His6X)* plasmids were transformed into *E. coli* Origami B (DE3) for recombinant protein production. Following purification, the proteins were analyzed by SDS-PAGE to assess their purity. Additionally, Western blot analysis was performed to confirm successful protein production and purification. SDS-PAGE results demonstrated the purity and integrity of the purified proteins (Fig. 12A). Western blotting revealed distinct 27 kDa bands corresponding to the sizes of HuScFvMT99/3^{WT}, HuScFvMT99/3^{BP}, and HuScFvMT99/3^{HY} (Fig. 12B).

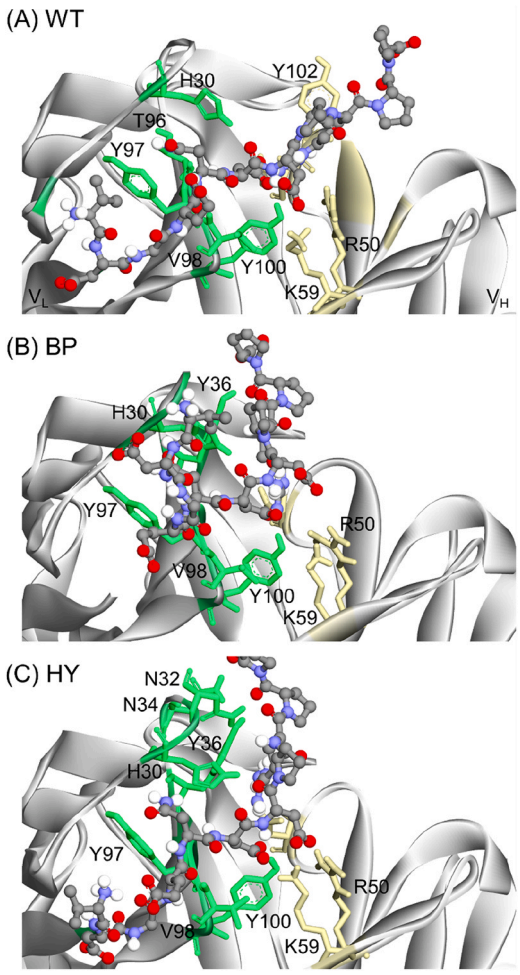

Fig. 9. Structural mapping of the binding interface obtained from the Prod phase MD simulations between HuScFvMT99/3, (A) WT, (B) BP, and (C) HY models, complex with CD99 peptide predicted models by AF3 method. The secondary structures of VH-VL domains and CD99 peptide are portrayed as white ribbons and ball-stick style, respectively. The interfacial residues of ScFv are annotated and shown in yellow (VH) and green (VL) sticks. Each interacting amino acid residue is highlighted in black-color labeled. The figure was drawn by Discovery Studio 2019 Client (Biovia software).

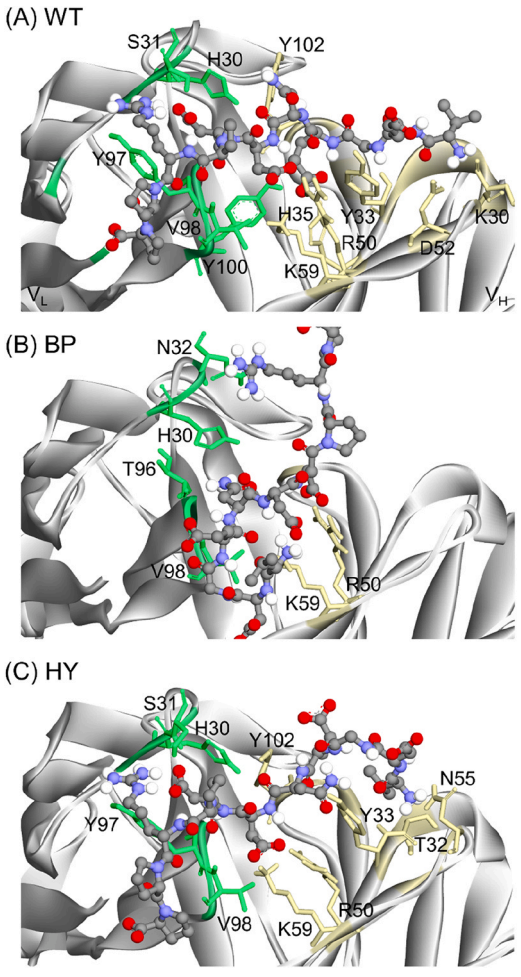

Fig. 10. Structural mapping of the binding interface obtained from the Prod phase MD simulations between HuScFvMT99/3, (A) WT, (B) BP, and (C) HY models, complex with CD99 peptide predicted models by HADDOCK method. The secondary structures of VH-VL domains and CD99 peptide are portrayed as white ribbons and ball-stick style, respectively. The interfacial residues of ScFv are annotated and shown in yellow (VH) and green (VL) sticks. Each interacting amino acid residue is highlighted in black-color labeled. The figure was drawn by Discovery Studio 2019 Client (Biovia software).

3.4. Binding activity and affinity of HuScFvMT99/3 variants against CD99 peptide

The binding activity of HuScFvMT99/3 variants against the CD99 peptide was assessed using ELISA, which demonstrated dose-dependent binding activity (Fig. 13A). HuScFvMT99/3^{WT} exhibited significantly higher binding activity compared to both HuScFvMT99/3^{BP} and HuScFvMT99/3^{HY}, with HuScFvMT99/3^{HY} showing the weakest binding activity. This phenomenon is particularly evident at 1 μg/mL of HuScFvs. Interestingly, at 5 μg/mL of HuScFvs, HuScFvMT99/3^{HY} showed partial recovery of binding activity compared to HuScFvMT99/3^{BP}. However, as ELISA only measures the end-point binding activity against the CD99 peptide, it does not fully capture the overall binding characteristics of HuScFvMT99/3. Therefore, BLI was employed to evaluate the binding kinetics of the HuScFvMT99/3 variants. The binding kinetic of the HuScFvMT99/3 variants are shown as sensorgrams (Fig. 13B). The kinetic parameters, including the association rate constant (K_{on}), dissociation rate constant (K_{off}), and equilibrium dissociation constant (K_D), are summarized in Table 4. Among the variants, HuScFvMT99/3^{BP} exhibited a faster off-rate (K_{off}) compared to both HuScFvMT99/3^{WT} and HuScFvMT99/3^{HY}. HuScFvMT99/3^{HY} displayed the highest K_D ($3.95 \pm 1.14 \times 10^{-7}$ M) compared to HuScFvMT99/3^{WT} ($1.35 \pm 0.59 \times 10^{-7}$ M) and HuScFvMT99/3^{BP} ($2.64 \pm 0.79 \times 10^{-7}$ M). Both ELISA and BLI assays confirmed consistent binding characteristics among the HuScFvMT99/3 variants.

3.5. Binding activity of HuScFvMT99/3 variants against CD99 on Jurkat T cells

The binding activity of the HuScFvMT99/3 variants to surface CD99 molecules on Jurkat T cells was evaluated using immunofluorescence staining. Flow cytometry analysis indicated that HuScFvMT99/3 variants were able to bind CD99 molecules on the surface of Jurkat T cells (Fig. 14A). While MFI from direct binding assay indicated the comparable binding level in HuScFvMT99/3^{WT} and HuScFvMT99/3^{BP}, the lowest MFI in HuScFvMT99/3^{HY} indicated worst binding activity, which correlates to ELISA and BLI result. Additionally, inhibition flow cytometry was performed to determine whether the HuScFvMT99/3 variants recognize CD99 on target cells at the same epitope as the CD99 peptide. The HuScFvMT99/3 variants specifically targeted CD99 on Jurkat T cells at the same epitope as the peptide, as evidenced by a reduction in binding activity to approximately 3–5 % (Fig. 14B). The

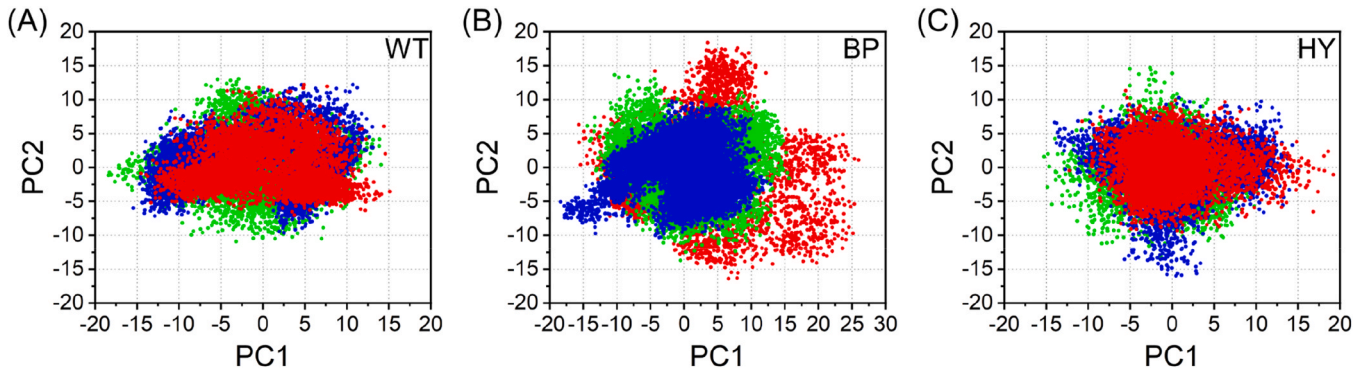

Fig. 11. Comparison of alternative modelling methods, AF2 (green), AF3 (blue), and HADDOCK (red) of PCA projection of the motion of Cα-atoms of HuScFvMT99/3 CD99 binding complexes. PCA profiles were obtained by plotting the first two principal components (PC1 and PC2) in the conformational space of the complexed HuScFvMT99/3 CD99 in (A) WT, (B) BP, and (C) HY. PC1 and PC2, respectively, represent a covariance matrix after elimination of eigenvectors.

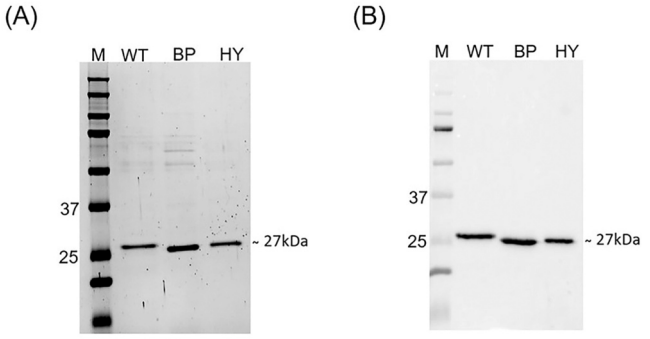

Fig. 12. Expression of HuScFvMT99/3 variants in *E. coli* Origami B (DE3). The 100 μg/mL of purified HuScFvMT99/3^{WT} (WT), HuScFvMT99/3^{BP} (BP), and HuScFvMT99/3^{HY} (HY) were subjected to SDS-PAGE (B) and western blot (C) under reducing condition. M represents the protein standard marker in kDa.

MFI from the direct binding and inhibition assays was used to calculate the percentage inhibition, which was 97.5 %, 93.5 %, and 95.26 % for HuScFvMT99/3^{WT}, HuScFvMT99/3^{BP}, and HuScFvMT99/3^{HY}, respectively (Fig. 14C). Notably, although HuScFvMT99/3^{BP} exhibited the lowest percentage inhibition, the MFI from direct binding flow cytometry indicated a binding level comparable to that of HuScFvMT99/3^{WT}.

4. Discussion

The potential of humanized antibodies for therapeutic applications is promising, as they closely resemble the properties of human antibodies. While these engineered molecules have revolutionized the treatment of various diseases, the occurrence of HAHA responses remains a significant challenge in the clinical development of humanized antibodies. [8] The HuScFvMT99/3 was recently developed and demonstrated retained immunoreactivity against CD99. [26] However, it is predicted to have high immunogenic potential. [24] These findings highlight the need for further optimization of the HuScFvMT99/3 sequence to improve its humanness and reduce its immunogenicity.

Humanization tools in antibody development are crucial for

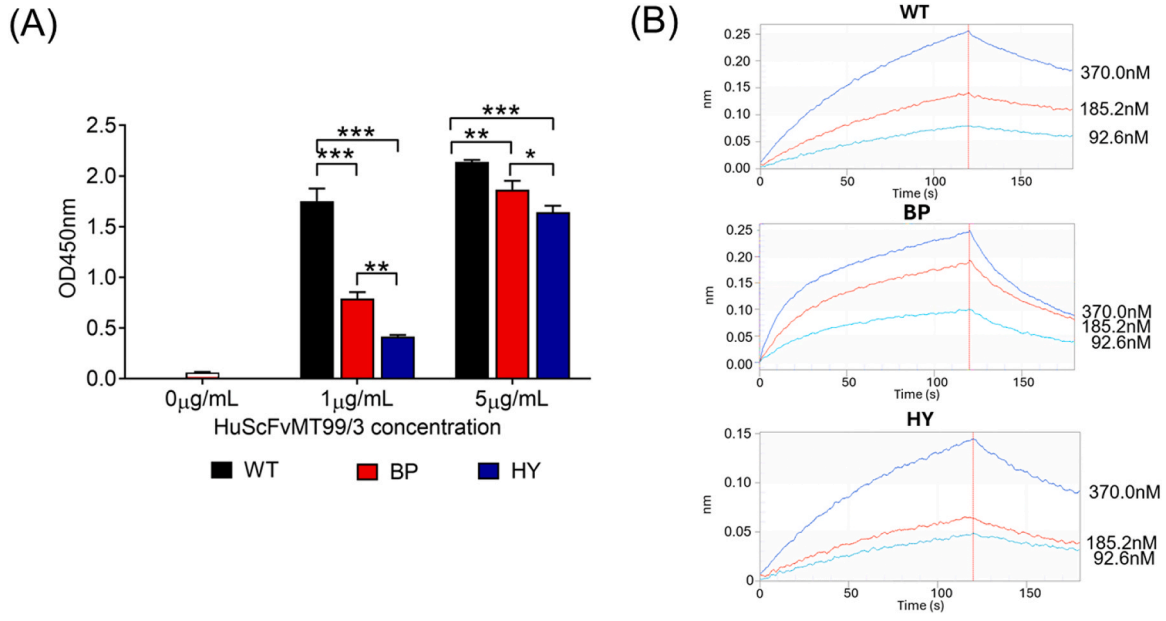

Fig. 13. Characterization of HuScFvMT99/3 variants activity. (A) The binding activity of HuScFvMT99/3 variants was determined using ELISA. Data represents mean ± SD from a triplicate experiment. The 0 μg/mL condition serves as the no-ScFv control. Statistical analysis was determined using One-way ANOVA. *p ≤ 0.05, *p ≤ 0.01, *p ≤ 0.001. (B) The kinetic binding of HuScFvMT99/3 variants at various concentrations was evaluated using BLI. The sensorgrams represent the data from triplicate experiments of each variant. WT, BP and HY represent HuScFvMT99/3^{WT}, HuScFvMT99/3^{BP} and HuScFvMT99/3^{HY}, respectively.

Table 4
Binding affinity analysis of HuScFvMT99/3 variants by BLI. The binding kinetic of HuScFvMT99/3 variants against CD99 peptide was evaluated by BLI. The K_{on}, K_{off}, and K_D were analyzed by Octet software.

	K_{on} (1/Ms)	K_{off} (1/s)	K_D(M)
HuScFvMT99/3^{WT}	$4.08\pm1.15\times10^{4}$	$4.89\pm5.77\times10^{-3}$	$1.35\pm0.59\times10^{-7}$
HuScFvMT99/3^{BP}	$6.05\pm0.18\times10^{4}$	$15.9\pm1.36\times10^{-3}$	$2.64\pm0.79\times10^{-7}$
HuScFvMT99/3^{HY}	$2.20\pm0.54\times10^{4}$	$8.06\pm0.95\times10^{-3}$	$3.95\pm1.14\times10^{-7}$

Note: The data was shown in mean ± SD from a triplicate experiment. Statistical analysis was determined using One-way ANOVA. *p ≤ 0.05, * **p < 0.001.

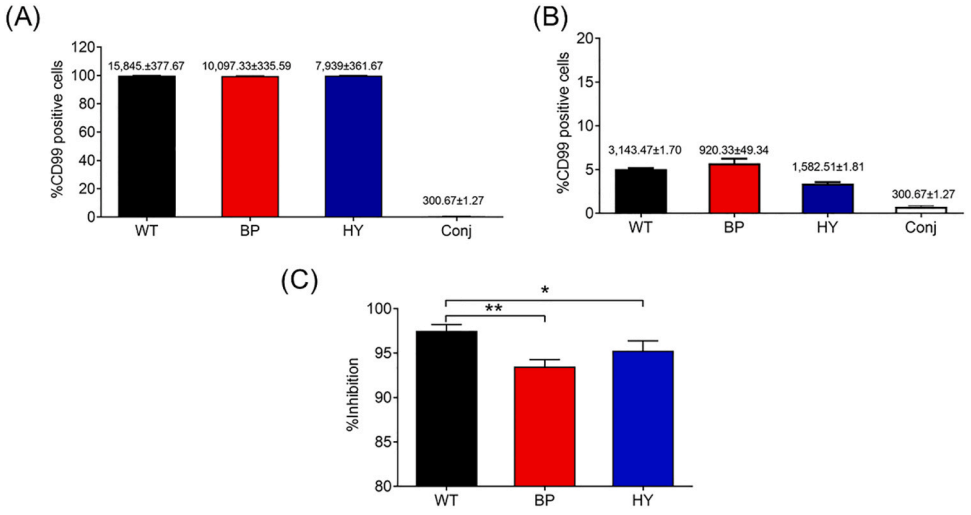

Fig. 14. Binding activity of HuScFvMT99/3 variants against CD99 in Jurkat T cells. (A) Direct binding of HuScFvMT99/3 variants against CD99 in Jurkat T cells was determined by flow cytometry. The percentage of CD99-positive cells is shown in the bar graph. (B) HuScFvMT99/3 variants were pre-incubated with CD99 peptide before being added to Jurkat T cells to determine binding inhibition. The MFI of direct binding and inhibition assay in mean ± SD from the triplicate experiment was noted above the bar graph. Conj represents conjugate control. (C) The MFI of direct binding and inhibition flow cytometry was used for % inhibition calculation. WT, BP and HY represent HuScFvMT99/3^{WT}, HuScFvMT99/3^{BP} and HuScFvMT99/3^{HY}, respectively. Data represents mean ± SD from triplicate experiments. Statistical analysis was determined by One-way ANOVA. * $p \leq 0.05$, * * $p \leq 0.01$.

reducing the immunogenicity of therapeutic antibodies derived from non-human sources. These tools employ various computational and experimental strategies to modify antibody sequences, making them more human-like. In this study, the humanness of HuScFvMT99/3 was improved by introducing amino acid mutations in the FRs using the BioPhi humanization platform [14], resulting in the HuScFvMT99/3^{BP} variant, which exhibited enhanced humanness compared to HuScFvMT99/3^{WT}. However, humanness evaluation by the T20 score analyzer and SAbPred indicated low humanness in the VL domain of the HuScFv. The discrepancy in humanness scores may arise from differences in the sequence database and training model employed by each humanization algorithm. [12–14] HuScFvMT99/3^{HY} was engineered by combining the VL^{WT} and VH^{BP} domains, resulting in an improved humanness score. RMSD analysis of the predicted HuScFvMT99/3 structures, using data from the RCSB PDB server, indicated high structural similarity among all HuScFvMT99/3 variants. Notably, the VL^{WT} domain in the HuScFVMT99/3^{HY} construct exhibited greater structural similarity to the WT than HuScFvMT99/3^{BP}. In contrast, the VH domains in the variants exhibited slightly lower structural similarity to HuScFvMT99/3^{WT}, likely due to the higher number of mutations in the VH framework regions near the CDRs. Immunogenicity predictions using PITHA indicated that, although HuScFvMT99/3^{HY} showed improved humanness, it still carries a high immunogenicity risk, similar to HuScFvMT99/3^{WT} and HuScFvMT99/3^{BP}. However, HuScFvMT99/3^{HY} features a larger cavity volume in the CDRs and a more hydrophobic CDR-H3 loop, suggesting a slight reduction in immunogenicity, thereby highlighting the effectiveness of the humanization process.

Accurate protein structure determination is crucial for improving humanness and understanding the biological activity of therapeutic antibodies. Using the deep-learning-based AF2 model [47,48], we constructed 3D structures for the VH and VL domains of HuScFvMT99/3. Based on diverse multiple sequence alignments [29]. variant models of HuScFvMT99/3 (WT, BP, and HY) were predicted. Although AF2 generates numerous confident predicted models, no specific pattern in secondary structure propensity was observed. The estimated RMSD values for the VH and VL domains calculated by the RCSB PDB server, closely resemble the WT model, which is expected, as both structures were derived from the same simulation framework. [49] Moreover, a z-score of the WT (VH = −6.46, VL = −5.17), BP (VH = −6.55, VL = −5.08), and HY (VH = −6.45, VL = −5.1) indicate that the modeled protein falls within the quality range of X-ray solved structures, supporting the improved humanness observed in the VH domain of the variant models (Fig. S3). The HuScFvMT99/3 structures were also

evaluated using the Verify3D server [50], which utilizes the DSSP algorithm to predict protein quality. This analysis showed that over 80 % of residues in these proteins exhibit a well-structured (data not shown).

As previously noted, proteins lacking templates in the Protein Data Bank may present challenges for accurate structure prediction using AF2. Therefore, to assess the reliability of the high-confidence models generated, all HuScFvMT99/3 VH and VL variants were subjected to MD simulations. The results of these simulations demonstrated that the predicted structures remained stable throughout the simulations. The RMSD (Fig. 4) and RMSF (Fig. 5) data provide insights into different structural characteristics. RMSD, which measures global stability, indicates that the HuScFvMT99/3^{BP} and HuScFvMT99/3^{HY} variants exhibit more stable VH-VL conformations than the WT. The WT structure, in contrast, shows a higher RMSD, which is likely attribute to increased flexibility in the CDRs that facilitates induced-fit binding. In contrast, RMSF analysis of local residue dynamics highlights notable alterations in the framework regions of the variants, attribute to amino acid substitutions. These substitutions can affect binding affinity by altering the spatial arrangement and interaction potential of the CDRs. This phenomenon, confirmed by the PCA method, showed that the HuScFvMT99/3 variants exhibited structural instability in the VH-VL domain compared to the WT. However, a balance between rigidity and flexibility is crucial for effective antibody binding. While flexibility in the CDR loops is necessary to accommodate diverse antigens, excessive variability can compromise binding interactions. [51,52] The AF2-predicted structures of the HuScFvMT99/3 VH and VL domains exhibit instability across each variant, however, these structures should be considered as a preliminary model. The observed instability may result from the presence of repeated sequences during the AF2 structural construction process, which could influence affect the overall prediction accuracy.

To assess potential biases in the AF2-predicted models, the HuScFvMT99/3 complex with the CD99 peptide was re-modeled using AF2 and compared to results from MD simulations and experimental studies. The predicted complex structures showed that all initial variant complexes preserved the same binding interface and CD99 peptide orientation, without inducing conformational changes in the CDR binding site (Table S1-S2, and Fig. S2). The binding interface primarily involves electrostatic interactions mediated by hydrophilic amino acid side chains. [53,54] After the simulations, our calculations showed there is substantial plasticity in the CDR loops as the variants that affect the molecular conformation of the binding interface residues can enhance binding affinity. As shown in Table 3, the main dividing force for the binding affinity were favorable changes in electrostatic (EEL) and van der Waals (vdW) interactions. [55,56] However, the $\Delta G_{binding}$ values for the AF2-predicted models did not align perfectly with the experimental results, particularly those from flow cytometry analysis. This discrepancy suggests that the AF2 method might introduce bias in the structural prediction, potentially impacting the modelling of ScFv-peptide complex structures. To address this, we employed alternative modeling approaches, including AF3 and HD, to model the HuScFvMT99/3-CD99 peptide complex, followed by MD simulations. Both AF3 and HD methods confidently predicted the complex's folded structures. The HuScFvMT99/3^{WT}-CD99 complex exhibited the highest binding activity and affinity against CD99. In contrast, the HuScFvMT99/3^{HY}-CD99 complex demonstrated an improved binding affinity and better humanness than the HuScFvMT99/3^{BP}-CD99 model. Although the modeling methods used in this study vary in their approaches to capturing known sequence-structure relationships, AF3 employs a simpler procedure for identifying homologous sequences than AF2. [30] The AF3 method displayed high confidence in predicting binding tendencies, particularly for multimeric complex models. This suggests that different deep learning-based structure prediction tools yield distinct predictive models, each with its strengths and limitations.

Considering the per-residue decomposition energy calculations (Fig. 7), our data suggest that the stability of the CDR VH domain, potentially influenced by FR mutations, plays a significant role in CD99-binding affinity. The results from the AF2 predictive modeling method contrast notably with the ELISA and BLI studies, particularly for the HuScFvMT99/3^{WT} complex, which exhibits weaker binding affinity. In contrast, the predicted complexes from the HD method revealed significant potential amino acid contributions from the CDR VH domain in both HuScFvMT99/3^{WT} and HuScFvMT99/3^{HY} complexes for CD99 binding, consistent with the experimental data. The simulation results indicated that HuScFvMT99/3^{WT} specifically enhanced the key residues Y33, H35, and R50, while HuScFvMT99/3^{HY} showed notable contributions from R50 and K59. These interactions were stronger at the CDR VH domain binding interfaces compared to the HuScFvMT99/3^{BP} variant. This suggests that the conserved sequence in the CDR VH domain underpins the binding activity of the humanized antibody. Additionally, coevolving residues within the CDRs often mediate protein recognition in multiprotein complexes, typically being spatially close and forming clusters of interacting residues. These findings imply a potential bias in the HuScFvMT99/3-CD99 complex model, which could affect structural predictions, highlighting the model's limitations despite the high confidence provided by AF2. The consistency between the per-residue decomposition energy from MD simulations and Prodigy predictions further supports this observation, even though the key amino acids at the binding interfaces of each system remain unchanged in the initial complex.

The confidence in the structures generated by AF2, at least in the present context, is low, which may be attributed to AF2's limited accuracy when predicting multimeric protein structures. Recent benchmarks indicate that the average success rate for predicting dimers is approximately 60 %, with accuracy decreasing as the number of chains increases. [29,57,58] REponse to these challenge, adapting the multiple sequence alignment information used in AF2 could potentially enhance the network's ability to outperform other protein docking methods, as it is currently trained primarily on single-chain data. [59,60]. Despite these limitations, the binding properties of the variant complexes (BP and HY) align with findings in antibody studies, where mutations that increase stability and rigidity often result in improved binding affinity. The evidence presented here suggests that AF2 models tend to misalign experimental results, as confirmed by MD simulations. When comparing the predicted HuScFvMT99/3^{WT} (WT-AF2) complex to the X-ray structure of the 10A1 Fab complex bound to the CD99 peptide (PDB ID: 7SFX) [23], we noted that (*i*) both the predicted and experimental epitopes bind within a cleft at the interface of the heavy and light chains; however (ii) sequence alignment (Fig. S4) reveals a relatively low similarity between the ScFv domains with an overlay score of 0.4353. The observed peptide segment adopts a left-handed helix, resembling other proline-rich motifs that form left-handed polyproline type-II helices. [61] Furthermore, this study proposes an integrated computational approach that combines structural insights with predictive deep-learning methods to enhance the humanness of therapeutic antibodies while minimizing risks to their efficacy and safety. It is important to note that the structural inspection alone may not be sufficient to fully capture the key binding interactions and activity of the antibody. Therefore, combining alternative deep learning-based structure prediction tools with MD simulations offers a more comprehensive understanding of potential structure-function relationships, grounded in experimental validation.

In this study, the amino acid residues of the FRs were modified using BioPhi, without altering the CDRs. Compared with HuScFvMT99/3^{WT}, the T20 score indicated a significant decrease in humanness for the VL domain of HuScFvMT99/3^{BP}, particularly when analyzing the full variable region (Table S3). This decrease in humanness is likely due to the grafting of mouse CDRs onto HuScFvMT99/3. These findings suggest that further improvement in the humanness of HuScFvMT99/3 could be achieved through CDR modification. Another humanization tool, abYsis [62], allows for more precise alterations of CDR residues to enhance the antibody humanness, overcoming some limitations of BioPhi.

Decomposed energy analysis using predicted structures from AF3 and HD highlighted critical amino acids in the CDRs involved in HuScFvMT99/3-CD99 interactions. Therefore, combining abYsis with decomposed energy data could support the modification of CDR residues to further improve the humanness of HuScFvMT99/3.

The HuScFvMT99/3 variants were successfully expressed in the *E. coli* system and were experimentally validated for binding activity using ELISA, and flow cytometry. All HuScFvMT99/3 variants demonstrated a specific binding against CD99 peptide. While both HuScFvMT99/3^{BP} and HuScFvMT99/3^{HY} demonstrated improved humanness, their binding activity was reduced compared to HuScFvMT99/3^{WT}. Despite HuScFvMT99/3^{HY} carrying the VL^{WT} domain, their binding activity against the CD99 peptide was not recovered. The binding affinity of HuScFvMT99/3 variants was also determined by BLI. Although the K_{on} is comparable, the faster dissociation rates for HuScFvMT99/3^{BP} and HuScFvMT99/3^{HY} contributed to lower overall binding affinity than WT. Nevertheless, HuScFvMT99/3^{BP} exhibits a nanomolar range of binding affinity, which is comparable to the previously reported potent anti-CD99 antibodies. [23,63] Additionally, the low-affinity antibody was found to exert cytotoxicity on cancer cells, and the reduced internalization by target cells in low-affinity variants may be advantageous for cancer therapeutic applications. [64] The binding activity of HuScFvMT99/3 variants was confirmed through flow cytometry. HuScFvMT99/3^{BP} exhibited comparable binding activity to the wild-type HuScFvMT99/3^{WT} against CD99 on target cells but was less inhibited by the CD99 peptide. Since surface CD99 reflects dynamic interactions and conformational flexibility, HuScFvMT99/3 may engage surface CD99 differently from it interacts with the CD99 peptide. This phenomenon highlights the efficacy of HuScFvMT99/3^{BP} in targeting the surface CD99, which is potentially developed as anti-CD99 therapeutic applications in the future.

While HuScFvMT99/3 variants were designed to improve humanness, the humanization process adversely affected their binding activity. Although BioPhi focuses on framework mutation, the modification could be introduced in the vernier zone. The phenylalanine 27 (F27) and asparagine 28 (N28) positions were identified as vernier zones in the VH domain of HuScFVMT99/3^{WT}. Modification of residues in antibody vernier zone can lead to alteration of CDRs loop structure, leading to impaired binding activity. [65,66] Antibody numbering schemes and CDR identification rules are also crucial for humanization. In this study, CDRs of HuScFvMT99/3 were identified based on Kabat's rules, which rely on sequence data to highlight key amino acids relevant to MD simulations and experimental data. While the Kabat numbering system relies solely on sequence alignment, it may overlook structurally important residues.[68] In this study, some VH residues were classified as CDRs based on alternative identification rules, despite amino acid mutations in the FRs. Thus, to preserve critical residues during humanization, it is essential to use numbering systems that incorporate structural context.

5. Conclusion

This study investigates the challenges of optimizing HuScFvMT99/3 using the BioPhi humanization platform to further enhance its humanness. While the modifications improve human similarity, they lead to a partial reduction in binding affinity for CD99. To explore the underlying factors, we examine structural stability and flexibility beyond the CDRs. AF2 and AF3 are employed to predict the 3D structure of the HuScFv-CD99 peptide complex, while HD is used to simulate their interactions. MD simulations assess the stability and flexibility of the complex over time. Additionally, PITHA and PCA utilize the immunogenicity and flexibility of the modified ScFvs. This comprehensive approach underscores the limitations of BioPhi in optimizing HuScFvMT99/3 and provides insights into the relationship between humanization and binding affinity, highlighting the potential of complex structure prediction for future improvements.

Funding

This research was supported by CMU Proactive Researcher, Chiang Mai University (Grant No. 1230/2567 to K. Sornsuwan), (Grant No. 744/2567 to O-a. Juntit), (Grant No. 768/2567 to K. Kodchakorn) and Fundamental Fund 2024 (R66EX01209) to C. Tayapiwatana.

CRediT authorship contribution statement

Kanchanok Kodchakorn: Writing – review & editing, Methodology, Formal analysis, Conceptualization. **Chatchai Tayapiwatana:** Supervision, Conceptualization. **Weeraya Thongkhum:** Methodology. **Nuchjira Takheaw:** Writing – review & editing. **Thanathat Pamonsupornwichit:** Writing – review & editing, Methodology, Formal analysis. **On-anong Juntit:** Methodology. **Kanokporn Sornsuwan:** Writing – review & editing, Writing – original draft, Methodology, Formal analysis.

Declaration of Competing Interest

The authors declare the following financial interests/personal relationships which may be considered as potential competing interests Chatchai Tayapiwatana, Ph.D. reports financial support was provided by Thailand Science Research and Innovation. Kanokporn Sornsuwan reports financial support was provided by Office of Research Administration, Chiang Mai University. On-anong Juntit reports financial support was provided by Office of Research Administration, Chiang Mai University. Kanchanok Kodchakorn reports financial support was provided by Office of Research Administration, Chiang Mai University. If there are other authors, they declare that they have no known competing financial interests or personal relationships that could have appeared to influence the work reported in this paper.

Acknowledgments

The authors would like to acknowledge Computational Simulation and Modelling Laboratory (CSML) and the Erawan HPC Project, Information Technology Service Center, Chiang Mai University, Chiang Mai, Thailand, for supporting and providing access to computing resources.

Appendix A. Supporting information

Supplementary data associated with this article can be found in the online version at doi:10.1016/j.csbj.2025.01.001.

Data availability

The data that support the findings of this study are available from the corresponding author upon reasonable request.

References

[1] Raja A, Kasana A, Verma V. Next-generation therapeutic antibodies for cancer treatment: advancements, applications, and challenges. Mol Biotechnol 2024.
[2] Jung SM, Kim WU. Targeted immunotherapy for autoimmune disease. Immune Netw 2022;22(1):e9.
[3] Lai Y, Dong C. Therapeutic antibodies that target inflammatory cytokines in autoimmune diseases. Int Immunol 2016;28(4):181–8.
[4] Chames P, Van Regenmortel M, Weiss E, Baty D. Therapeutic antibodies: successes, limitations and hopes for the future. Br J Pharm 2009;157(2):220–33.
[5] Lo BK. Antibody humanization by CDR grafting. Methods Mol Biol 2004;248:135–59.
[6] Maadi H, Soheilifar MH, Choi WS, Moshtaghian A, Wang Z. Trastuzumab mechanism of action; 20 years of research to unravel a dilemma. Cancers 2021;13(14).
[7] Ogata A, Tanaka T. Tocilizumab for the treatment of rheumatoid arthritis and other systemic autoimmune diseases: current perspectives and future directions. Int J Rheuma 2012;2012:946048.

[8] Welt S, Ritter G, Williams Jr C, et al. Preliminary report of a phase I study of combination chemotherapy and humanized A33 antibody immunotherapy in patients with advanced colorectal cancer. Clin Cancer Res 2003;9(4):1347–53.
[9] Kushner BH, Cheung IY, Modak S, Basu EM, Roberts SS, Cheung N-K. Humanized 3F8 anti-GD2 monoclonal antibody dosing with granulocyte-macrophage colony-stimulating factor in patients with resistant neuroblastoma: a phase 1 clinical trial. JAMA Oncol 2018;4(12):1729–35.
[10] Hummer AM, Deane CM. Designing stable humanized antibodies. Nat Biomed Eng 2024;8(1):3–4.
[11] Gordon GL, Raybould MIJ, Wong A, Deane CM. Prospects for the computational humanization of antibodies and nanobodies. Front Immunol 2024;15:1399438.
[12] Gao SH, Huang K, Tu H, Adler AS. Monoclonal antibody humanness score and its applications. BMC Biotechnol 2013;13(1):55.
[13] Marks C, Hummer AM, Chin M, Deane CM. Humanization of antibodies using a machine learning approach on large-scale repertoire data. Bioinform 2021;37(22):4041–7.
[14] Prihoda D, Maamary J, Waight A, et al. BioPhi: a platform for antibody design, humanization, and humanness evaluation based on natural antibody repertoires and deep learning. mAbs 2022;14(1):2020203.
[15] Yamashita T. Toward rational antibody design: recent advancements in molecular dynamics simulations. Int Immunol 2018;30(4):133–40.
[16] Zhang D, Chen CF, Zhao BB, et al. A novel antibody humanization method based on epitopes scanning and molecular dynamics simulation. PloS One 2013;8(11):e80636.
[17] Margreitter C, Mayrhofer P, Kunert R, Oostenbrink C. Antibody humanization by molecular dynamics simulations—in-silico guided selection of critical backmutations 2016;29(6):266–75.
[18] Pamonsupornwichit T, Kodchakorn K, Udomwong P, et al. Engineering affinity of humanized ScFv targeting CD147 antibody: a combined approach of mCSM-AB2 and molecular dynamics simulations. J Mol Graph Model 2024;133:108884.
[19] Watson RL, Buck J, Levin LR, et al. Endothelial CD99 signals through soluble adenylyl cyclase and PKA to regulate leukocyte transendothelial migration. J Exp Med 2015;212(7):1021–41.
[20] Pasello M, Manara MC, Scotlandi K. CD99 at the crossroads of physiology and pathology. J Cell Commun Signal 2018;12(1):55–68.
[21] Baldauf MC, Orth MF, Dallmayer M, et al. Robust diagnosis of Ewing sarcoma by immunohistochemical detection of super-enhancer-driven EWSR1-ETS targets. Oncotarget 2018;9(2):1587–601.
[22] Guerzoni C, Fiori V, Terracciano M, et al. CD99 triggering in Ewing sarcoma delivers a lethal signal through p53 pathway reactivation and cooperates with doxorubicin. Clin Cancer Res 2015;21(1):146–56.
[23] Romero LA, Hattori T, Ali MAE, et al. High-valency anti-CD99 antibodies toward the treatment of T cell acute lymphoblastic leukemia. J Mol Biol 2022;434(5):167402.
[24] Khunkaewla P, Chiampanichayakul S, Yasamut U, Pata S, Kasinrerk W. Production, characterization, and functional analysis of newly established CD99 monoclonal antibodies MT99/1 and MT99/2. Hybridoma 2007;26(4):241–50.
[25] Sahagan BG, Dorai H, Saltzgaber-Muller J, et al. A genetically engineered murine/human chimeric antibody retains specificity for human tumor-associated antigen. J Immunol 1986;137(3):1066–74.
[26] Takheaw N, Pamonsupornwichit T, Chaiwut R, et al. Exploring the biological activity of a humanized anti-CD99 ScFv and antibody for targeting T cell malignancies 2024;14(11):1422.
[27] Yin R, Pierce BG. Evaluation of AlphaFold antibody-antigen modeling with implications for improving predictive accuracy. Protein Sci 2024;33(1):e4865.
[28] Du K., Huang H. Development of anti-PD-L1 antibody based on structure prediction of AlphaFold2. 2023;14.
[29] Jumper J, Evans R, Pritzel A, et al. Highly accurate protein structure prediction with AlphaFold. Nature 2021;596(7873):583–9.
[30] Abramson J, Adler J, Dunger J, et al. Accurate structure prediction of biomolecular interactions with AlphaFold 3. Nature 2024;630(8016):493–500.
[31] Honorato RV, Trellet ME, Jiménez-García B, et al. The HADDOCK2.4 web server for integrative modeling of biomolecular complexes. Nat Protoc 2024;19(11):3219–41.
[32] Varadi M, Bertoni D, Magana P, et al. AlphaFold protein structure database in 2024: providing structure coverage for over 214 million protein sequences. Nucleic Acids Res 2024;52(D1):D368–75.
[33] Bittrich S, Segura J, Duarte JM, Burley SK, Rose Y. RCSB protein data bank: exploring protein 3D similarities via comprehensive structural alignments. Bioinform 2024;40(6):btae370.
[34] Xue LC, Rodrigues JP, Kastritis PL, Bonvin AM, Vangone A. PRODIGY: a web server for predicting the binding affinity of protein–protein complexes. Bioinform 2016;32(23):3676–8.
[35] Vangone A, Bonvin AMJJ. Contacts-based prediction of binding affinity in protein–protein complexes. eLife 2015;4:e07454.
[36] Liang S, Zhang C. Prediction of immunogenicity for humanized and full human therapeutic antibodies. PloS One 2020;15(8):e0238150.
[37] Case DA, Aktulga HM, Belfon K, et al. AmberTools. J Chem Inf Model 2023;63(20):6183–91.
[38] Tian C, Kasavajhala K, Belfon KAA, et al. ff19SB: amino-acid-specific protein backbone parameters trained against quantum mechanics energy surfaces in solution. J Chem Theory Comput 2020;16(1):528–52.
[39] Götz AW, Williamson MJ, Xu D, Poole D, Le Grand S, Walker RC. Routine microsecond molecular dynamics simulations with amber on gpus. 1. generalized born. J Chem Theory Comput 2012;8(5):1542–55.
[40] Salomon-Ferrer R, Götz AW, Poole D, Le Grand S, Walker RC. Routine microsecond molecular dynamics simulations with AMBER on GPUs. 2. explicit solvent particle mesh ewald. J Chem Theory Comput 2013;9(9):3878–88.
[41] Roe DR, Cheatham TE. 3rd. PTRAJ and CPPTRAJ: software for processing and analysis of molecular dynamics trajectory data. J Chem Theory Comput 2013;9(7):3084–95.
[42] Wang E, Sun H, Wang J, et al. End-point binding free energy calculation with MM/PBSA and MM/GBSA: strategies and applications in drug design. Chem Rev 2019;119(16):9478–508.
[43] David CC, Jacobs DJ. Principal component analysis: a method for determining the essential dynamics of proteins. Methods Mol Biol 2014;1084:193–226.
[44] Martinez AM, Kak AC. PCA versus LDA. IEEE PAMI 2001;23(2):228–33.
[45] Kodchakorn K, Kongtawelert P. Molecular dynamics study on the strengthening behavior of Delta and Omicron SARS-CoV-2 spike RBD improved receptor-binding affinity. PloS One 2022;17(11):e0277745.
[46] Di Mambro T, Vanzolini T, Bianchi M, et al. Development and in vitro characterization of a humanized scFv against fungal infections. PloS One 2022;17(10):e0276786.
[47] Kryshtafovych A, Schwede T, Topf M, Fidelis K, Moult J. Critical assessment of methods of protein structure prediction (CASP)-Round XIV. Proteins 2021;89(12):1607–17.
[48] Frank C., Khoshouei A., de Stigter Y., et al. Efficient and scalable de novo protein design using a relaxed sequence space. *bioRxiv*. 2023:2023.2002.2024.529906.
[49] Mariani V, Biasini M, Barbato A, Schwede T. lDDT: a local superposition-free score for comparing protein structures and models using distance difference tests. Bioinform 2013;29(21):2722–8.
[50] Lüthy R, Bowie JU, Eisenberg D. Assessment of protein models with three-dimensional profiles. Nature 1992;356(6364):83–5.
[51] Manjula S, Sivanandam M, Kumaradhas P. Probing the "fingers" domain binding pocket of Hepatitis C virus NS5B RdRp and D559G resistance mutation via molecular docking, molecular dynamics simulation and binding free energy calculations. J Biomol Struct Dyn 2019;37(9):2440–56.
[52] Chen J, Wang J, Zhu W. Molecular mechanism and energy basis of conformational diversity of antibody SPE7 revealed by molecular dynamics simulation and principal component analysis. Sci Rep 2016;6(1):36900.
[53] Krissinel E. Crystal contacts as nature's docking solutions. J Comput Chem 2010;31(1):133–43.
[54] Krissinel E, Henrick K. Inference of macromolecular assemblies from crystalline state. J Mol Biol 2007;372(3):774–97.
[55] Wang Y, Liu M, Gao J. Enhanced receptor binding of SARS-CoV-2 through networks of hydrogen-bonding and hydrophobic interactions. Proc Natl Acad Sci USA 2020;117(25):13967–74.
[56] Kodchakorn K, Chokepaichitkool T, Kongtawelert P. Mutational scanning of spike RBD protein for enhanced ACE2 affinity emerging Southeast Asia in the late transmission phase. Sci Rep 2022;12(1):5896.
[57] Mukherjee S, Zhang Y. MM-align: a quick algorithm for aligning multiple-chain protein complex structures using iterative dynamic programming. Nucleic Acids Res 2009;37(11):e83.
[58] Zhu W, Shenoy A, Kundrotas P, Elofsson A. Evaluation of alphafold-multimer prediction on multi-chain protein complexes. Bioinform 2023;39(7).
[59] Bryant P, Pozzati G, Elofsson A. Improved prediction of protein-protein interactions using AlphaFold2. Nat Commun 2022;13(1):1265.
[60] Burke DF, Bryant P, Barrio-Hernandez I, et al. Towards a structurally resolved human protein interaction network. Nat Struct Mol Biol 2023;30(2):216–25.
[61] Freund C, Schmalz HG, Sticht J, Kühne R. Proline-rich sequence recognition domains (PRD): ligands, function and inhibition. Handb Exp Pharm 2008;186:407–29.
[62] Swindells MB, Porter CT, Couch M, et al. abYsis: integrated antibody sequence and structure—management, analysis, and prediction. J Mol Biol 2017;429(3):356–64.
[63] Fiori V., Doninici S., Moricoli D., et al., Inventors; Diatheva SRL, assignee. Anti-cd99 diabody or igg antibody and uses thereof. US patent EP3801771B1. 2024/02/14, 2024,.
[64] Wong OK, Tran TT, Ho WH, et al. RN765C, a low affinity EGFR antibody drug conjugate with potent anti-tumor activity in preclinical solid tumor models. Oncotarget 2018;9(71):33446–58.
[65] Foote J, Winter G. Antibody framework residues affecting the conformation of the hypervariable loops. J Mol Biol 1992;224(2):487–99.
[66] Caldas C, Coelho V, Kalil J, Moro AM, Maranhão AQ, Brígido MM. Humanization of the anti-CD18 antibody 6.7: an unexpected effect of a framework residue in binding to antigen. Mol Immunol 2003;39(15):941–52.